

Article

## Photophysical Property and Photocatalytic Activity of New $Gd_2InSbO_7$ and $Gd_2FeSbO_7$ Compounds under Visible Light Irradiation

Jingfei Luan \* and Yong Xu

State Key Laboratory of Pollution Control and Resource Reuse, School of the Environment, Nanjing University, Nanjing 210093, Jiangsu, China; E-Mail: xuscute2006@163.com

\* Author to whom correspondence should be addressed; E-Mail: jfluan@nju.edu.cn; Tel.: +86-135-8520-6718; Fax: +86-25-8370-7304.

Received: 3 December 2012; in revised form: 21 December 2012 / Accepted: 24 December 2012 / Published: 7 January 2013

---

**Abstract:**  $Gd_2InSbO_7$  and  $Gd_2FeSbO_7$  were synthesized first, and their structural and photocatalytic properties were studied. The lattice parameters and the band gaps for  $Gd_2InSbO_7$  and  $Gd_2FeSbO_7$  were 10.449546 Å, 10.276026 Å, 2.897 eV and 2.151 eV. The photocatalytic degradation of rhodamine B was performed with  $Gd_2InSbO_7$  and  $Gd_2FeSbO_7$  under visible light irradiation.  $Gd_2InSbO_7$  and  $Gd_2FeSbO_7$  had higher catalytic activity compared with  $Bi_2InTaO_7$ .  $Gd_2FeSbO_7$  exhibited higher catalytic activity than  $Gd_2InSbO_7$ . The photocatalytic degradation of rhodamine B followed with the first-order reaction kinetics, and the first-order rate constant  $k$  was 0.01606, 0.02220 or 0.00329  $\text{min}^{-1}$  with  $Gd_2InSbO_7$ ,  $Gd_2FeSbO_7$  or  $Bi_2InTaO_7$  as photocatalyst. Complete removal of rhodamine B was observed after visible light irradiation for 225 min or 260 min with  $Gd_2FeSbO_7$  or  $Gd_2InSbO_7$  as photocatalyst. The evolution of  $CO_2$  was realized, and it indicated continuous mineralization of rhodamine B during the photocatalytic process. The possible photocatalytic degradation pathway of rhodamine B was proposed.

**Keywords:** inorganic compounds; crystal growth; X-ray diffraction; catalytic properties; optical properties

---

## 1. Introduction

Nowadays, with the development of industry, wastewater is yielded in bulk. Particularly, some industries, such as textile and dyeing manufacturing, produce a large amount of dyestuff wastewater [1]. These dyestuffs are usually synthetic aromatic compounds, which are seriously harmful to the aquatic biota. Moreover, the coloration of the wastewater in streams or lakes would absolutely influence the solar illumination, which would affect the growth of creatures and hydrophytes. Among all kinds of dyestuff, rhodamine B (RhB) is one of the most important representatives of xanthene dyes. RhB is toxic and resistant to biodegradation and direct photolysis, thus RhB would have a considerable deleterious effect upon the environmental matrix. RhB undergoes natural reductive anaerobic degradation; as a result, potentially carcinogenic aromatic amines [2,3] are yielded. Moreover, RhB is widely used as a photosensitizer, a quantum counter and an active medium in dye lasers, *etc.* [4,5]. Thus, we use RhB as a probe contaminant to evaluate the activity of new photocatalysts, both under ultraviolet light and visible light irradiation.

In terms of the enormous harm of RhB dye wastewater, it was thoroughly urgent to remove RhB dye from effluents before they were emitted to natural water bodies. At present, several treatment measurements were adopted for RhB dye removal. For example, the technology of adsorption using absorbents [3,6–8], such as activated carbon, has been found to be an efficient technology for decolorization of wastewater. Although it was quite effective for activated carbon to adsorb RhB dye in wastewater, activated carbon was restricted from use because of its high cost and difficulty in being regenerated. Therefore, a novel processing method, photocatalysis, has been developed for removing RhB dye wastewater. Photocatalysis is an advanced oxidation processes and has aroused more and more attention by investigators [9–23], and much scientific research on the photocatalytic degradation of aqueous organic contaminants has been reported [10–31]. Some investigations [2,32–38] about the photodegradation of RhB have been reported under ultraviolet light or visible light irradiation, showing that photocatalysis was an effective degradation method for degrading dye to a large extent.

With the development of the investigation of the photocatalysis process, investigators also paid much attention to researching and developing novel photocatalysts [39–43]. Presently,  $\text{TiO}_2$  was the most common photocatalyst; however,  $\text{TiO}_2$  could not be used in the visible light region and could only degrade RhB under ultraviolet light irradiation. Moreover, ultraviolet light only occupied 4% of sunlight, which was a restrained factor for photocatalysis technology with  $\text{TiO}_2$  as the catalyst. Therefore, some efficient catalysts, which could generate electron-hole pairs under visible light irradiation, should be developed, because visible light occupies 43% of sunlight. Fortunately,  $\text{A}_2\text{B}_2\text{O}_7$  compounds were often considered to have photocatalytic properties under visible light irradiation. In our previous work [44], we have found that  $\text{Bi}_2\text{InTaO}_7$  crystallized with the pyrochlore-type structure and acted as a photocatalyst under visible light irradiation and seemed to have a potential for improvement of the photocatalytic activity upon modification of its structure. Based on the above analysis, we could assume that substitution of  $\text{Ta}^{5+}$  by  $\text{Sb}^{5+}$ , substitution of  $\text{Bi}^{3+}$  by  $\text{Gd}^{3+}$  and substitution of  $\text{In}^{3+}$  by  $\text{Fe}^{3+}$  in  $\text{Bi}_2\text{InTaO}_7$  might increase carrier concentration; as a result, the new photocatalysts  $\text{Gd}_2\text{InSbO}_7$  and  $\text{Gd}_2\text{FeSbO}_7$  might have advanced photocatalytic properties.  $\text{Gd}_2\text{InSbO}_7$  and  $\text{Gd}_2\text{FeSbO}_7$  were never synthesized before and never used in the photocatalysis progress. The molecular composition of  $\text{Gd}_2\text{InSbO}_7$  and  $\text{Gd}_2\text{FeSbO}_7$  was very similar with other  $\text{A}_2\text{B}_2\text{O}_7$  compounds.

Thus, the resemblance suggested that  $\text{Gd}_2\text{InSbO}_7$  and  $\text{Gd}_2\text{FeSbO}_7$  might possess photocatalytic properties under visible light irradiation, which was similar with the other members in the  $\text{A}_2\text{B}_2\text{O}_7$  family. This paper reported the preparation process and property characterization of  $\text{Gd}_2\text{InSbO}_7$  and  $\text{Gd}_2\text{FeSbO}_7$ . Both  $\text{Gd}_2\text{InSbO}_7$  and  $\text{Gd}_2\text{FeSbO}_7$  were semiconductor compounds that were synthesized for the first time. In this contribution, we discussed the structural and photocatalytic properties of  $\text{Gd}_2\text{InSbO}_7$  and  $\text{Gd}_2\text{FeSbO}_7$  by degrading RhB under visible light irradiation and compared the photocatalytic activity among  $\text{Gd}_2\text{InSbO}_7$ ,  $\text{Gd}_2\text{FeSbO}_7$  and  $\text{Bi}_2\text{InTaO}_7$  in order to elucidate the structure-photocatalytic activity relationship in these newly synthesized compounds.

## 2. Results and Discussion

### 2.1. Characterization

Figure 1a,b show the SEM images of  $\text{Gd}_2\text{InSbO}_7$  and  $\text{Gd}_2\text{FeSbO}_7$  with low magnification. Figure 1c,d show the TEM images of  $\text{Gd}_2\text{InSbO}_7$  and  $\text{Gd}_2\text{FeSbO}_7$  with high magnification. The results showed that the particle diameter of  $\text{Gd}_2\text{FeSbO}_7$  was 240 nm and the particle diameter of  $\text{Gd}_2\text{InSbO}_7$  was 310 nm. The nanosized particles of  $\text{Gd}_2\text{FeSbO}_7$  and  $\text{Gd}_2\text{InSbO}_7$  were obtained, and these particles were in inhomogenous global shapes. Figure 1 revealed that the average particle size of  $\text{Gd}_2\text{FeSbO}_7$  was smaller than that of  $\text{Gd}_2\text{InSbO}_7$ . There were two reasons to obtain nanocrystals in this experiment, while synthesizing  $\text{Gd}_2\text{InSbO}_7$  and  $\text{Gd}_2\text{FeSbO}_7$  powders by the solid-state method. Firstly, the powders, which were obtained after a sintering process by an electric furnace, would be ground by mortar three times and then would be ground in a ball mill three times. The total time for grinding the above photocatalyst powders was approximately 15 h. Secondly, the sizes of the photocatalyst particles were different. We utilized a centrifuge to realize separation of the photocatalyst particles, which had different sizes by adjusting the rotation speed of the centrifuge, and the small particles were obtained. SEM-EDS spectrum taken from the prepared  $\text{Gd}_2\text{FeSbO}_7$  indicated the existence of gadolinium, iron, antimony and oxygen. As to the prepared  $\text{Gd}_2\text{InSbO}_7$ , gadolinium, indium, antimony and oxygen were detected and other elements were not identified.

**Figure 1.** (a) Scanning electron microscope (SEM) image of  $\text{Gd}_2\text{InSbO}_7$  with low magnification; (b) SEM image of  $\text{Gd}_2\text{FeSbO}_7$  with low magnification; (c) Transmission electron microscopy (TEM) image of  $\text{Gd}_2\text{InSbO}_7$  with high magnification; (d) TEM image of  $\text{Gd}_2\text{FeSbO}_7$  with high magnification; (e) The selected area electron diffraction (SAED) pattern of  $\text{Gd}_2\text{InSbO}_7$ ; (f) The SAED pattern of  $\text{Gd}_2\text{FeSbO}_7$ .

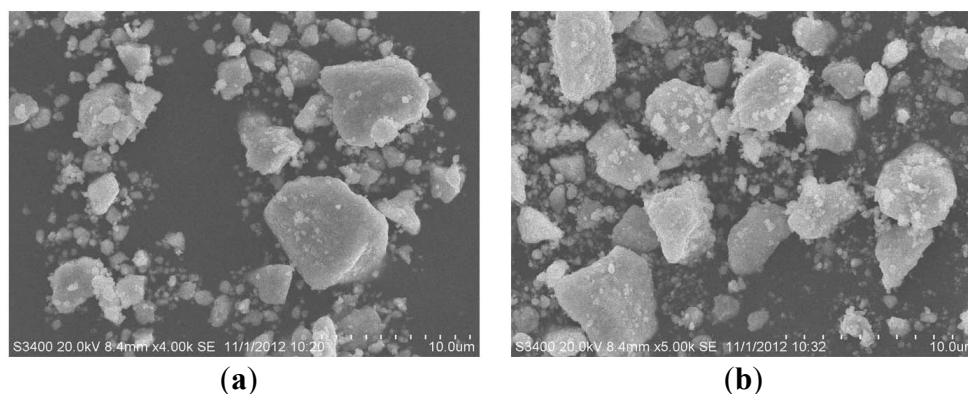
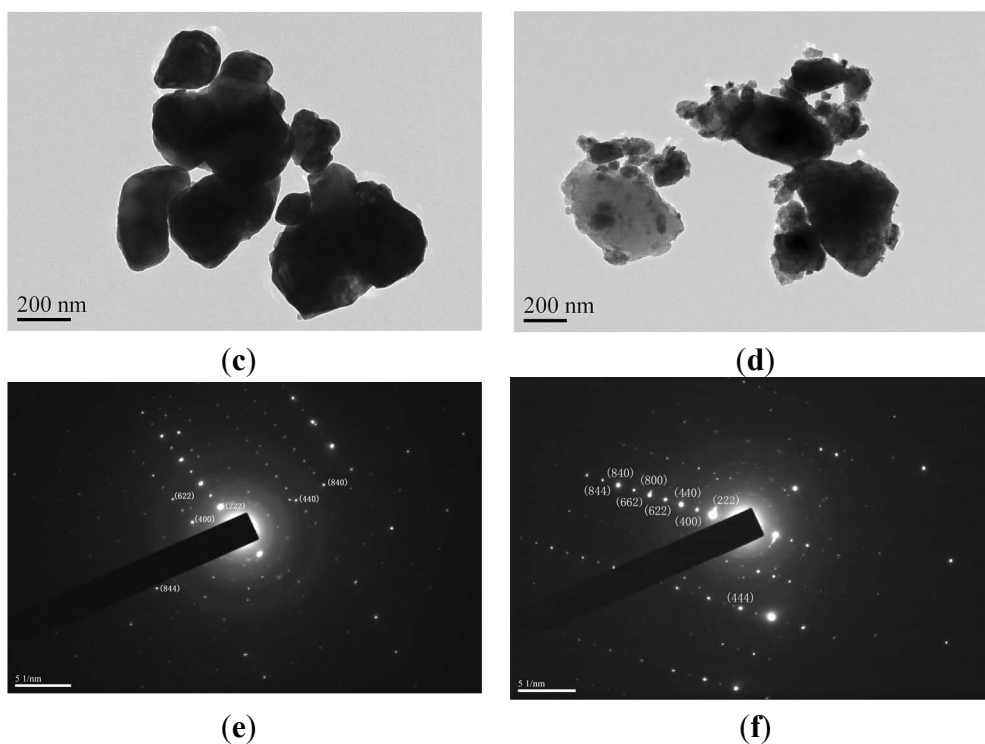
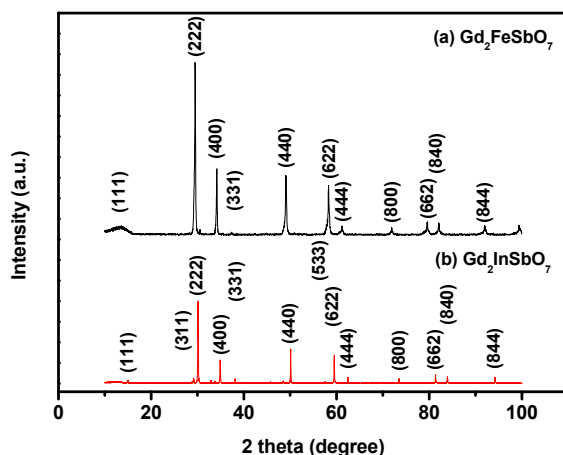
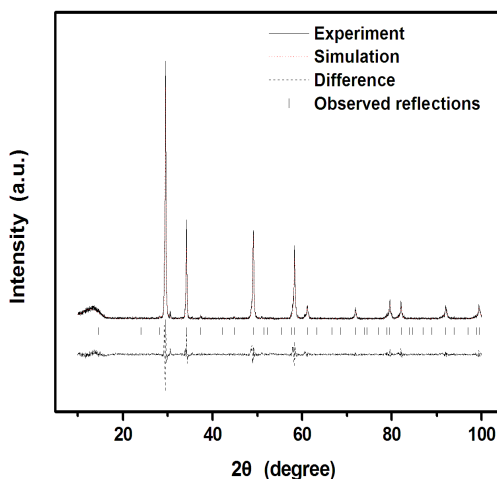


Figure 1. Cont.



X-ray powder diffraction patterns of  $\text{Gd}_2\text{FeSbO}_7$  and  $\text{Gd}_2\text{InSbO}_7$  are shown in Figure 2. Figure 3 displays the powder X-ray diffraction patterns of  $\text{Gd}_2\text{InSbO}_7$  together with full-profile structure refinements of the collected data as obtained by the RIETAN<sup>TM</sup> [45] program, which is based on Rietveld analysis. The results of the final refinement for  $\text{Gd}_2\text{FeSbO}_7$  and  $\text{Gd}_2\text{InSbO}_7$  manifested an excellent consistency between the observed and calculated intensities for the pyrochlore-type structure, a cubic crystal system and a space group  $Fd\bar{3}m$  (O atoms were included in the model). The lattice parameters of  $\text{Gd}_2\text{InSbO}_7$  and  $\text{Gd}_2\text{FeSbO}_7$  were  $10.449546 \text{ \AA}$  and  $10.276026 \text{ \AA}$ , respectively. All the diffraction peaks for  $\text{Gd}_2\text{FeSbO}_7$  and  $\text{Gd}_2\text{InSbO}_7$  could be successfully indexed based on the lattice constant and above space group. The atomic coordinates and structural parameters of  $\text{Gd}_2\text{FeSbO}_7$  and  $\text{Gd}_2\text{InSbO}_7$  are listed in Tables 1 and 2, respectively. In addition, Our XRD results showed that  $\text{Gd}_2\text{FeSbO}_7$  and  $\text{Gd}_2\text{InSbO}_7$  crystallized with the same structure, and 2 theta angles of each reflection of  $\text{Gd}_2\text{InSbO}_7$  changed with the substitution of  $\text{In}^{3+}$  by  $\text{Fe}^{3+}$ . The lattice parameter decreased from  $a = 10.449546 \text{ \AA}$  for  $\text{Gd}_2\text{InSbO}_7$  to  $a = 10.276026 \text{ \AA}$  for  $\text{Gd}_2\text{FeSbO}_7$ , indicating a decrease in the lattice parameter of the photocatalyst with the decrease of M ionic radii,  $\text{Fe}^{3+} (0.78 \text{ \AA}) < \text{In}^{3+} (0.92 \text{ \AA})$ . Figure 1e,f show the selected area electron diffraction patterns of  $\text{Gd}_2\text{InSbO}_7$  and  $\text{Gd}_2\text{FeSbO}_7$ , respectively. It could be seen that  $\text{Gd}_2\text{InSbO}_7$  and  $\text{Gd}_2\text{FeSbO}_7$  crystallized with a cubic crystal system, and the lattice parameters  $a$  of  $\text{Gd}_2\text{InSbO}_7$  and  $\text{Gd}_2\text{FeSbO}_7$  were proved to be  $10.449546 \text{ \AA}$  and  $10.276026 \text{ \AA}$ , respectively. According to the calculation results from Figure 1e,f the main diffraction peaks (222), (440), (400) and (622) for  $\text{Gd}_2\text{InSbO}_7$  and  $\text{Gd}_2\text{FeSbO}_7$  could be found and indexed within Figure 1e,f.

**Figure 2.** X-ray powder diffraction patterns of (a)  $Gd_2FeSbO_7$  and (b)  $Gd_2InSbO_7$ .**Figure 3.** X-ray powder diffraction patterns and Rietveld refinements of  $Gd_2InSbO_7$  prepared by a solid-state reaction method at 1320 °C. A difference (observed-calculated) profile is shown beneath. The tic marks represent reflection positions.**Table 1.** Structural parameters of  $Gd_2FeSbO_7$  prepared by the solid state reaction method.

Atom	<i>x</i>	<i>y</i>	<i>z</i>	Occupation factor
Gd	0.00000	0.00000	0.00000	1.0
Fe	0.50000	0.50000	0.50000	0.5
Sb	0.50000	0.50000	0.50000	0.5
O(1)	-0.20249	0.12500	0.12500	1.0
O(2)	0.12500	0.12500	0.12500	1.0

**Table 2.** Structural parameters of  $Gd_2InSbO_7$  prepared by the solid state reaction method.

Atom	<i>x</i>	<i>y</i>	<i>z</i>	Occupation factor
Gd	0.00000	0.00000	0.00000	1.0
In	0.50000	0.50000	0.50000	0.5
Sb	0.50000	0.50000	0.50000	0.5
O(1)	-0.15469	0.12500	0.12500	1.0
O(2)	0.12500	0.12500	0.12500	1.0

Our X-ray diffraction outcomes showed that  $Gd_2FeSbO_7$ ,  $Gd_2InSbO_7$  and  $Bi_2InTaO_7$  crystallized with the same pyrochlore-type structure. The cubic system structure with space group  $Fd\bar{3}m$  for  $Bi_2InTaO_7$  remained unchanged, with  $Ta^{5+}$  being substituted by  $Sb^{5+}$  and with  $Bi^{3+}$  being substituted by  $Gd^{3+}$ . The cubic system structure with space group  $Fd\bar{3}m$  for  $Bi_2InTaO_7$  also remained unchanged with  $Ta^{5+}$  being substituted by  $Sb^{5+}$ , with  $In^{3+}$  being substituted by  $Fe^{3+}$  and with  $Bi^{3+}$  being substituted by  $Gd^{3+}$ . The result of refinements for  $Gd_2FeSbO_7$  generated the unweighted  $R$  factors,  $R_p = 16.20\%$  with space group  $Fd\bar{3}m$ . Similarly, the result of refinements for  $Gd_2InSbO_7$  generated the unweighted  $R$  factors,  $R_p = 12.13\%$  with space group  $Fd\bar{3}m$ . Zou *et al.* [46] refined the crystal structure of  $Bi_2InNbO_7$  and obtained a large  $R$  factor, which was owing to a slightly modified structure model for  $Bi_2InNbO_7$ . Based on the high purity of the precursors that were used in this study and the EDS results that did not trace any other elements, it was unlikely that the observed space groups originated from the presence of impurities. Therefore, it was suggested that the slightly high  $R$  factor for  $Gd_2FeSbO_7$  or  $Gd_2InSbO_7$  was due to a slightly modified structure model of  $Gd_2FeSbO_7$  or  $Gd_2InSbO_7$ . It should be emphasized that the defects or the disorder/order of a fraction of the atoms could result in the change of structures, including different bond-distance distributions, thermal displacement parameters and/or occupation factors for some of the atoms.

The XPS spectra of  $Gd_2FeSbO_7$  and  $Gd_2InSbO_7$  were obtained. The various elemental peaks, which are corresponding to specific binding energies, are given in Table 3. The results further suggested that the oxidative valence state of Gd, Fe, Sb and O ions from  $Gd_2FeSbO_7$  were +3, +3, +5 and -2, respectively. For  $Gd_2FeSbO_7$ , the mean atomic ratios of Gd: Fe: Sb: O were 2.00: 1.02: 0.99: 6.96 based on averaging our XPS, SEM-EDS and XFS results. Similarly, the oxidation state of Gd, In, Sb and O ions from  $Gd_2InSbO_7$  were +3, +3, +5 and -2, respectively. For  $Gd_2InSbO_7$ , the mean atomic ratios of Gd: In: Sb: O were 2.00: 1.03: 0.97: 6.98 based on averaging our XPS, SEM-EDS and XFS results. Consequently, it could be deduced that the final materials were of high purity under our preparation conditions. It was noteworthy that neither shoulders nor widening of any XPS peaks of  $Gd_2FeSbO_7$  or  $Gd_2InSbO_7$  were observed, suggesting the absence of any other phases.

**Table 3.** Binding energies (BE) for key elements.

$In_{3d5/2}$ BE (eV)	$Sb_{3d5/2}$ BE (eV)	$Fe_{2p3/2}$ BE (eV)	$Gd_{4d5/2}$ BE (eV)	$O_{1s}$ BE (eV)
	530.85	710.81	143.93	530.35
444.65	530.82		143.85	530.12

Figures 4 and 5 present the absorption spectra of  $Gd_2FeSbO_7$  and  $Gd_2InSbO_7$ , respectively. In contrast to the well-known  $TiO_2$ , whose absorption edge was less than 380 nm, the absorption edges of newly synthesized  $Gd_2FeSbO_7$  and  $Gd_2InSbO_7$  were found to be 586 nm and 428 nm, respectively, which were in the visible region of the spectrum. It was noteworthy that the apparent absorption (defined hereby as 1-transmission) could not take into consideration reflection and scattering. As a result, the apparent absorbance at sub-bandgap wavelengths (600 to 800 nm for  $Gd_2FeSbO_7$  and 425 to 800 nm for  $Gd_2InSbO_7$ ) was higher than zero.

For a crystalline semiconductor compound, the optical absorption near the band edge followed the equation [47,48]:  $ah\nu = A (h\nu - E_g)^n$ . Here,  $A$ ,  $\alpha$ ,  $E_g$  and  $\nu$  denoted proportional constant, absorption

coefficient, band gap and light frequency, respectively. In this equation,  $n$  determined the character of the transition in a semiconductor compound.  $E_g$  and  $n$  could be calculated by the following steps: (i) plotting  $\ln(ah\nu)$  versus  $\ln(h\nu - E_g)$  assuming an approximate value of  $E_g$ , (ii) deducing the value of  $n$  based on the slope in this graph and (iii) refining the value of  $E_g$  by plotting  $(ah\nu)^{1/n}$  versus  $h\nu$  and extrapolating the plot to  $(ah\nu)^{1/n} = 0$ . According to this method, Figure 6 shows the plot of  $(ah\nu)^{1/n}$  versus  $h\nu$  for  $Gd_2FeSbO_7$  and  $Gd_2InSbO_7$ . It was evidently to be found from Figure 6 that the values of  $E_g$  for  $Gd_2FeSbO_7$  and  $Gd_2InSbO_7$  were calculated to be 2.151 eV and 2.897 eV, respectively, while the values of  $n$  for  $Gd_2FeSbO_7$  and  $Gd_2InSbO_7$  were calculated to be 0.50 and 0.50, respectively, indicating that  $Gd_2FeSbO_7$  possessed a narrower band gap compared with that of  $Gd_2InSbO_7$ .

**Figure 4.** Upper trace: action spectra of rhodamine B degradation with  $Gd_2FeSbO_7$  as catalyst under visible light irradiation. Lower trace: absorption spectra of  $Gd_2FeSbO_7$ .

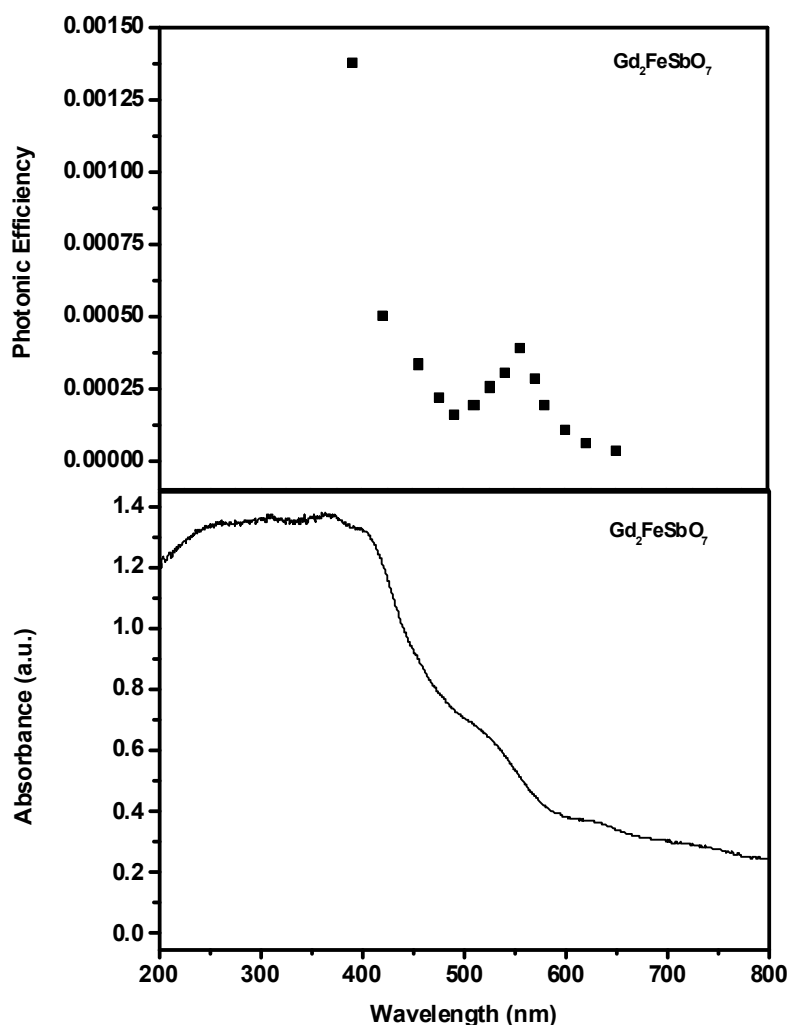


**Figure 5.** Upper trace: action spectra of rhodamine B degradation with  $Gd_2InSbO_7$  as catalyst under visible light irradiation. Lower trace: absorption spectra of  $Gd_2InSbO_7$ .

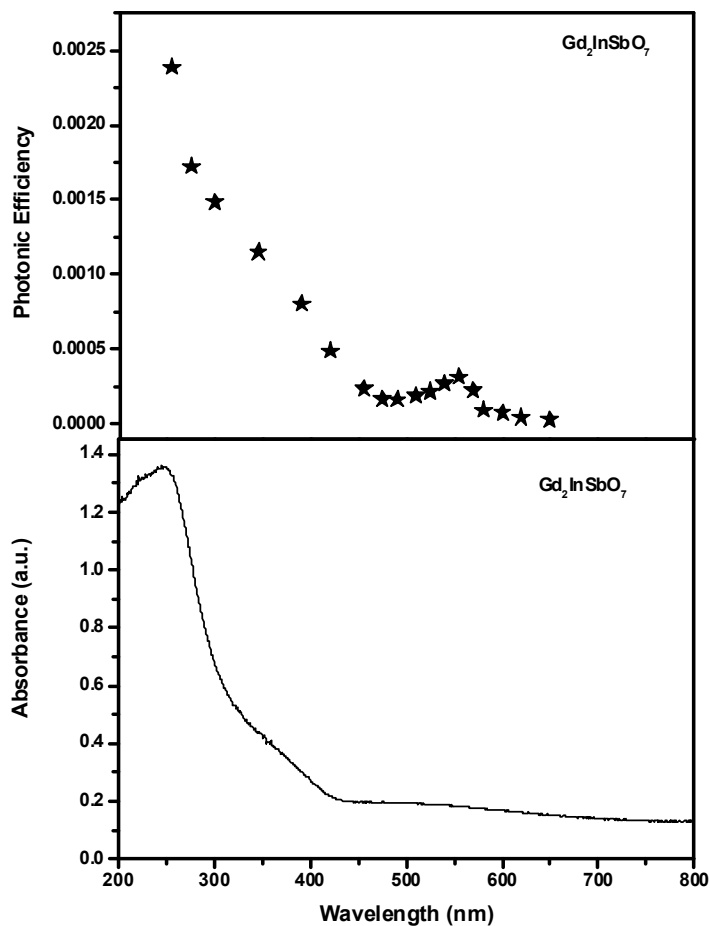
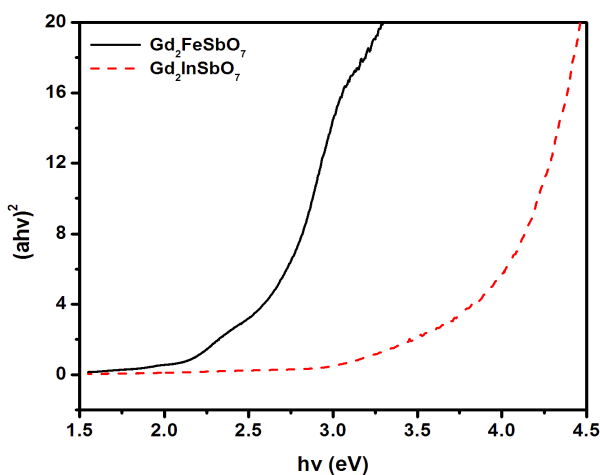


**Figure 6.** Plot of  $(ahv)^2$  versus  $hv$  for  $Gd_2FeSbO_7$  and  $Gd_2InSbO_7$ .

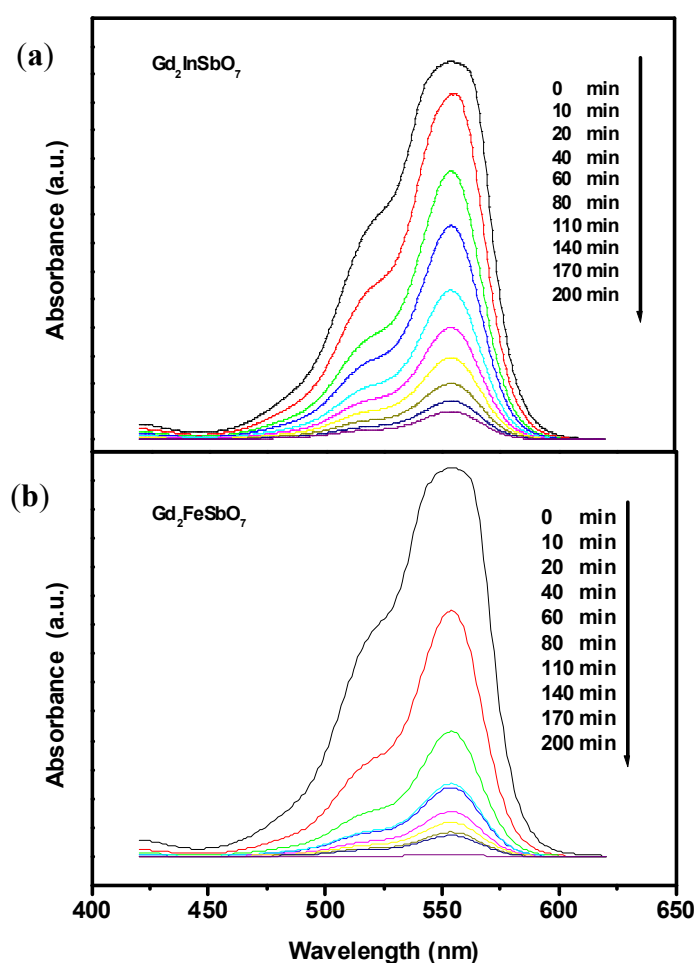


### 2.2. Photocatalytic Activity

Generally, the photocatalytic process by semiconductors begins with the direct absorption of supra-bandgap photons and the generation of electron–hole pairs within semiconductor particles. This is followed by diffusion of the charge carriers to the surface of the semiconductor particle. Changes in

the UV-Vis spectrum of rhodamine B (RhB) upon exposure to visible light ( $\lambda > 400$  nm) with the presence of  $\text{Gd}_2\text{FeSbO}_7$  or  $\text{Gd}_2\text{InSbO}_7$  are depicted in Figure 7a,b, respectively. The measurements were performed under oxygen-saturation conditions ( $[\text{O}_2]_{\text{sat}} = 1.02 \times 10^{-3}$  M). The degradation of RhB did not occur in darkness within the  $\text{Gd}_2\text{FeSbO}_7/\text{RhB}$  suspension or  $\text{Gd}_2\text{InSbO}_7/\text{RhB}$  suspension or  $\text{Bi}_2\text{InTaO}_7/\text{RhB}$  suspension or RhB suspension. It could be seen from Figure 7a and Figure 7b that a reduction of typical RhB peaks at 553.5 nm and 525 nm was clearly noticed. The results showed that the initial degradation rate of RhB was about  $2.413 \times 10^{-9}$  mol  $\text{L}^{-1}$   $\text{s}^{-1}$ , and the initial photonic efficiency was estimated to be 0.05069% ( $\lambda = 420$  nm) for  $\text{Gd}_2\text{FeSbO}_7$ . Similarly, the initial degradation rate of RhB was about  $2.322 \times 10^{-9}$  mol  $\text{L}^{-1}$   $\text{s}^{-1}$ , and the initial photonic efficiency was estimated to be 0.04877% ( $\lambda = 420$  nm) for  $\text{Gd}_2\text{InSbO}_7$ . For  $\text{Bi}_2\text{InTaO}_7$ , after visible light irradiation for 200 min, the RhB concentration decreased only from 0.0293 mM to 0.0161 mM, and the initial degradation rate of RhB was about  $1.1 \times 10^{-9}$  mol  $\text{L}^{-1}$   $\text{s}^{-1}$ . The initial photonic efficiency was estimated to be 0.02311% ( $\lambda = 420$  nm) for  $\text{Bi}_2\text{InTaO}_7$ . By contrast, the photonic efficiency of  $\text{Bi}_2\text{InTaO}_7$  was inferior to that of  $\text{Gd}_2\text{FeSbO}_7$  or  $\text{Gd}_2\text{InSbO}_7$ .

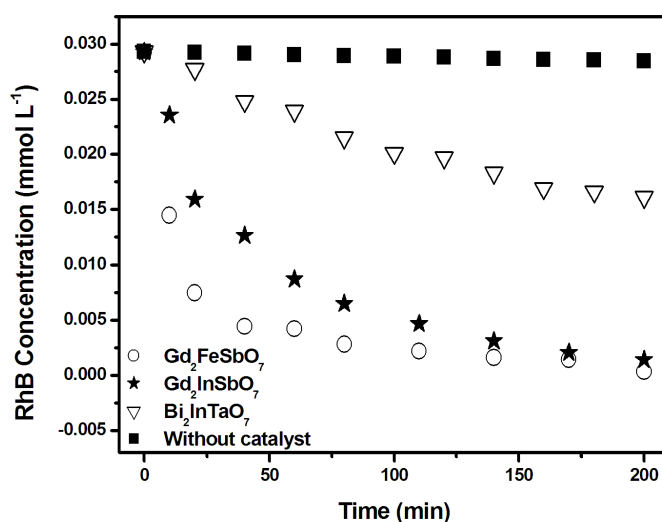
**Figure 7.** Temporal spectral changes of aqueous rhodamine B due to visible light irradiation in the presence of (a)  $\text{Gd}_2\text{InSbO}_7$  or (b)  $\text{Gd}_2\text{FeSbO}_7$ .



The kinetics of RhB degradation deduced according to the spectral changes under visible light irradiation are shown in Figure 8, which describes the kinetics not only with  $\text{Gd}_2\text{FeSbO}_7$ ,  $\text{Gd}_2\text{InSbO}_7$

and  $\text{Bi}_2\text{InTaO}_7$  as catalysts, but also without any photocatalyst. As expected, reduction of RhB signal in the controlled measurements in the absence of a photocatalyst was promising. In addition, the photodegradation removal rate of RhB was 90.35%, 77.80% and 26.62% after visible light irradiation for 80 min with  $\text{Gd}_2\text{FeSbO}_7$ ,  $\text{Gd}_2\text{InSbO}_7$  and  $\text{Bi}_2\text{InTaO}_7$  as catalysts, respectively. Complete removal of rhodamine B was observed after visible light irradiation for 225 min or 260 min with  $\text{Gd}_2\text{FeSbO}_7$  or  $\text{Gd}_2\text{InSbO}_7$  as photocatalyst. Based on the above outcomes, it was much faster for  $\text{Gd}_2\text{FeSbO}_7$  and  $\text{Gd}_2\text{InSbO}_7$  to photodegrade RhB compared with  $\text{Bi}_2\text{InTaO}_7$ , and the photocatalytic degradation activity of  $\text{Gd}_2\text{FeSbO}_7$  or  $\text{Gd}_2\text{InSbO}_7$  for degrading RhB was higher than that of  $\text{Bi}_2\text{InTaO}_7$ ; moreover,  $\text{Gd}_2\text{FeSbO}_7$  showed higher photocatalytic degradation activity than  $\text{Gd}_2\text{InSbO}_7$ . The main reason was that the lattice parameter  $a = 10.746410 \text{ \AA}$  for  $\text{Bi}_2\text{InTaO}_7$  was larger than the lattice parameter  $a = 10.449546 \text{ \AA}$  for  $\text{Gd}_2\text{InSbO}_7$ , and the lattice parameter  $a = 10.449546 \text{ \AA}$  for  $\text{Gd}_2\text{InSbO}_7$  was larger than the lattice parameter  $a = 10.276026 \text{ \AA}$  for  $\text{Gd}_2\text{FeSbO}_7$ , which probably resulted in a decrease for the migration distance of photogenerated electrons and holes to reach the reaction site on the photocatalyst surface; subsequently, the creation of more active sites was realized. As a result, it would probably improve the photocatalytic activities by decreasing the lattice parameter of the photocatalyst.

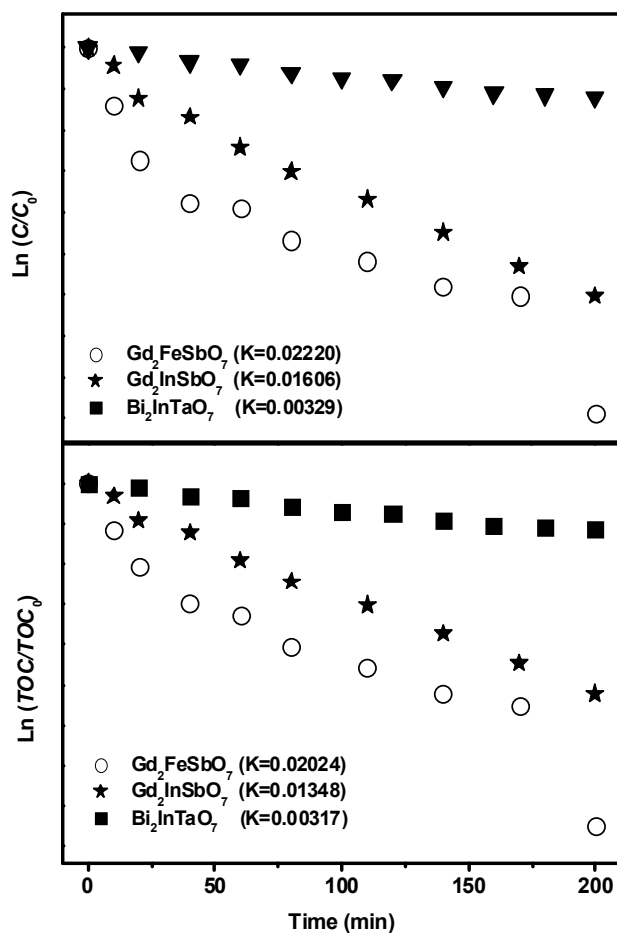
**Figure 8.** Photocatalytic degradation of rhodamine B under visible light irradiation in the presence of  $\text{Gd}_2\text{FeSbO}_7$ ,  $\text{Gd}_2\text{InSbO}_7$ ,  $\text{Bi}_2\text{InTaO}_7$ , as well as in the absence of a photocatalyst.



The first order nature of the photocatalytic degradation kinetics with  $\text{Gd}_2\text{FeSbO}_7$ ,  $\text{Gd}_2\text{InSbO}_7$  and  $\text{Bi}_2\text{InTaO}_7$  as catalysts is clearly exhibited in Figure 9, which describes a linear correlation between  $\ln(C/C_0)$  (or  $\ln(\text{TOC}/\text{TOC}_0)$ ) and the irradiation time for the photocatalytic degradation of RhB under visible light irradiation by using  $\text{Gd}_2\text{FeSbO}_7$  or  $\text{Gd}_2\text{InSbO}_7$  or  $\text{Bi}_2\text{InTaO}_7$  as catalyst. Here,  $C$  represented the RhB concentration at time  $t$ , and  $C_0$  represented the initial concentration of RhB.  $\text{TOC}$  represented the total organic carbon concentration at time  $t$ , and  $\text{TOC}_0$  denoted the initial total organic carbon concentration. According to the relationship between  $\ln(C/C_0)$  and the irradiation time, the apparent first-order rate constant  $k$  was estimated to be  $0.02220 \text{ min}^{-1}$  with  $\text{Gd}_2\text{FeSbO}_7$  as catalyst,  $0.01606 \text{ min}^{-1}$  with  $\text{Gd}_2\text{InSbO}_7$  as catalyst and  $0.00329 \text{ min}^{-1}$  with  $\text{Bi}_2\text{InTaO}_7$  as catalyst, indicating that  $\text{Gd}_2\text{FeSbO}_7$  and  $\text{Gd}_2\text{InSbO}_7$  were more effective than  $\text{Bi}_2\text{InTaO}_7$  for the photocatalytic degradation

of RhB under visible light irradiation. Meanwhile,  $\text{Gd}_2\text{FeSbO}_7$  showed more effective photocatalytic activity for degrading RhB than  $\text{Gd}_2\text{InSbO}_7$ . According to the relationship between  $\ln(\text{TOC}/\text{TOC}_0)$  and the irradiation time, the apparent first-order rate constant  $k$  was estimated to be  $0.02024 \text{ min}^{-1}$  with  $\text{Gd}_2\text{FeSbO}_7$  as catalyst,  $0.01348 \text{ min}^{-1}$  with  $\text{Gd}_2\text{InSbO}_7$  as catalyst and  $0.00317 \text{ min}^{-1}$  with  $\text{Bi}_2\text{InTaO}_7$  as catalyst, indicating that the photodegradation intermediate products of RhB were probably produced during the photocatalytic degradation of RhB under visible light irradiation.

**Figure 9.** Observed first-order kinetic plots for the photocatalytic degradation of rhodamine B with  $\text{Gd}_2\text{FeSbO}_7$ ,  $\text{Gd}_2\text{InSbO}_7$  or  $\text{Bi}_2\text{InTaO}_7$  as catalyst under visible light irradiation.



The photodegradation intermediate products of RhB in our experiment were identified as succinic acid ( $m/z = 118$ ), terephthalic acid ( $m/z = 166$ ), pentanedioic acid, 3-Hydroxybenzoic acid ( $m/z = 138$ ), 1,2-benzenedicarboxylic acid and maleic acid ( $m/z = 116$ ). Based on the intermediate products detected in this work, a possible photocatalytic degradation pathway for RhB is proposed in Figure 10. This pathway was similar, but not identical, to the pathway proposed by Horikoshi *et al.* [49] for the photodegradation of RhB under ultraviolet light illumination assisted by microwave radiation with  $\text{TiO}_2$  as catalyst. According to the research from Zhang *et al.* [32], the photodegradation of RhB occurred through two competitive processes: one was *N*-demethylation and the other one was the destruction of the conjugated structure. Thus, we considered that chromophore cleavage, opening-ring and mineralization would be the main photocatalytic degradation pathway of RhB in our experiment.

RhB was converted to smaller organic species, which were ultimately mineralized into inorganic products, such as  $\text{CO}_2$  and water. Figure 11 shows  $\text{CO}_2$  yields during the photocatalytic degradation of RhB with  $\text{Gd}_2\text{FeSbO}_7$ ,  $\text{Gd}_2\text{InSbO}_7$  or  $\text{Bi}_2\text{InTaO}_7$  as catalyst under visible light irradiation. The results indicated that the yielded  $\text{CO}_2$  increased gradually with the increase of reaction time by using  $\text{Gd}_2\text{FeSbO}_7$ ,  $\text{Gd}_2\text{InSbO}_7$  or  $\text{Bi}_2\text{InTaO}_7$  as catalyst. The production rate of  $\text{CO}_2$  with  $\text{Gd}_2\text{FeSbO}_7$  or  $\text{Gd}_2\text{InSbO}_7$  as catalyst was higher than that with  $\text{Bi}_2\text{InTaO}_7$  as catalyst, which was in line with the absorption curves (Figures 4 and 5) of  $\text{Gd}_2\text{FeSbO}_7$  and  $\text{Gd}_2\text{InSbO}_7$ . For example, after visible light irradiation for 200 min, the  $\text{CO}_2$  production was 0.2366 mmol with  $\text{Gd}_2\text{FeSbO}_7$  as catalyst, 0.2280 mmol with  $\text{Gd}_2\text{InSbO}_7$  as catalyst and 0.1080 mmol with  $\text{Bi}_2\text{InTaO}_7$  as catalyst.

**Figure 10.** Suggested photocatalytic degradation pathway scheme for rhodamine B under visible light irradiation in the presence of  $\text{Gd}_2\text{FeSbO}_7$  or  $\text{Gd}_2\text{InSbO}_7$ .

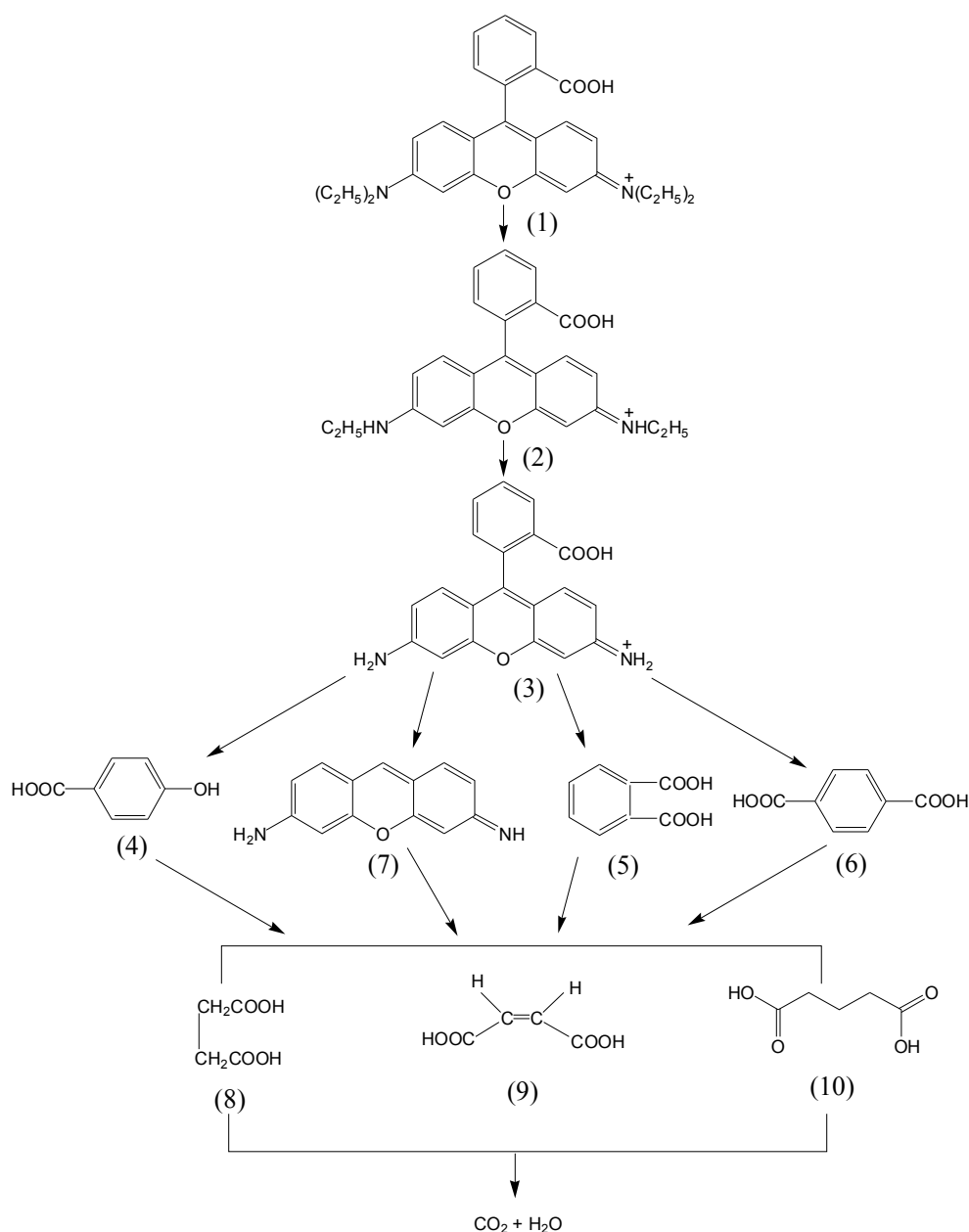


**Figure 11.** CO<sub>2</sub> production kinetics during the photocatalytic degradation of rhodamine B with Gd<sub>2</sub>FeSbO<sub>7</sub>, Gd<sub>2</sub>InSbO<sub>7</sub> or Bi<sub>2</sub>InTaO<sub>7</sub> as catalyst under visible light irradiation.

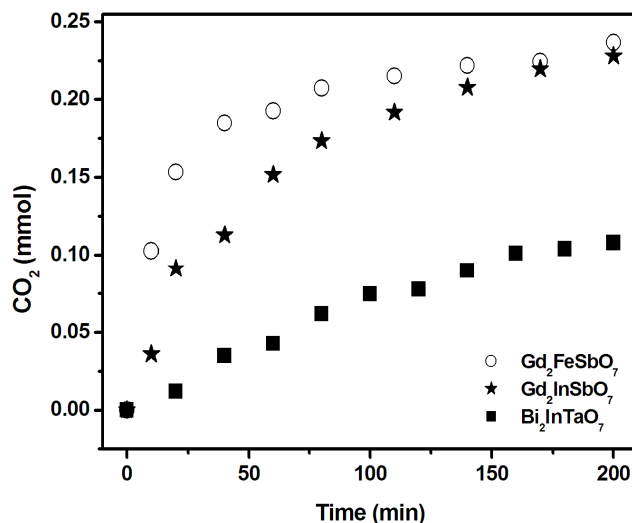
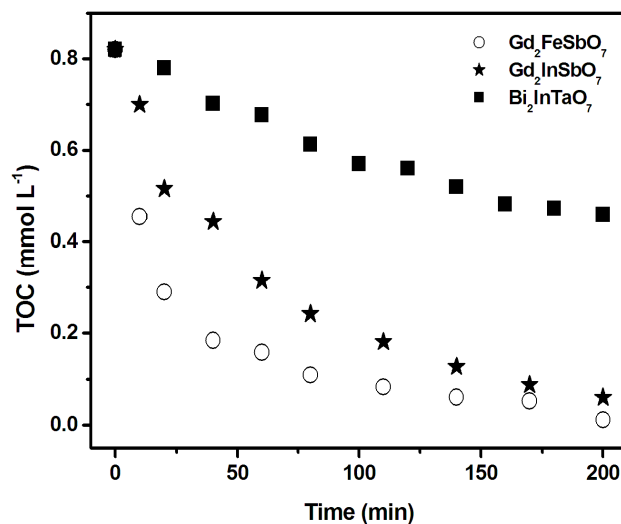


Figure 12 shows the change of the total organic carbon (TOC) for photocatalytic degradation of rhodamine B during visible light irradiation with Gd<sub>2</sub>FeSbO<sub>7</sub>, Gd<sub>2</sub>InSbO<sub>7</sub> or Bi<sub>2</sub>InTaO<sub>7</sub> as catalyst. The TOC measurements revealed the disappearance of organic carbon when the RhB solution containing Gd<sub>2</sub>FeSbO<sub>7</sub>, Gd<sub>2</sub>InSbO<sub>7</sub> or Bi<sub>2</sub>InTaO<sub>7</sub> was exposed under visible light irradiation. The results showed that 86.70%, 70.49% or 25.26% of TOC decrease was obtained after visible light irradiation for 80 min with Gd<sub>2</sub>FeSbO<sub>7</sub>, Gd<sub>2</sub>InSbO<sub>7</sub> or Bi<sub>2</sub>InTaO<sub>7</sub> as catalyst, respectively. The turnover numbers, which were the ratio between total amount of evolved gas and exhausted catalyst, were calculated to be more than 0.18 or 0.19 for Gd<sub>2</sub>FeSbO<sub>7</sub> or Gd<sub>2</sub>InSbO<sub>7</sub> after 200 min of reaction time under visible light irradiation. The reactions ceased when the light was turned off, indicating an obvious photic response.

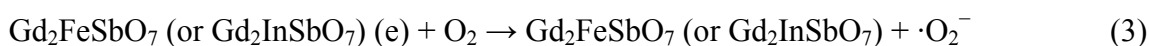
**Figure 12.** Disappearance of the total organic carbon (TOC) during the photocatalytic degradation of rhodamine B with Gd<sub>2</sub>FeSbO<sub>7</sub>, Gd<sub>2</sub>InSbO<sub>7</sub> or Bi<sub>2</sub>InTaO<sub>7</sub> as catalyst under visible light irradiation.



The photocatalytic performance of  $\text{Gd}_2\text{FeSbO}_7$  and  $\text{Gd}_2\text{InSbO}_7$  was remarkable under visible light irradiation. This superior quality could be even more bracing if one considered the fact that the specific surface areas of  $\text{Gd}_2\text{FeSbO}_7$  and  $\text{Gd}_2\text{InSbO}_7$  were further smaller than that of titanium dioxide. In this experiment, BET isotherm measurements gave a specific surface area of  $4.12 \text{ m}^2 \text{ g}^{-1}$ ,  $3.26 \text{ m}^2 \text{ g}^{-1}$  and  $1.26 \text{ m}^2 \text{ g}^{-1}$  for  $\text{Gd}_2\text{FeSbO}_7$ ,  $\text{Gd}_2\text{InSbO}_7$  and  $\text{Bi}_2\text{InTaO}_7$ , respectively, which was almost 12-times smaller than that of  $\text{TiO}_2$  ( $46.24 \text{ m}^2 \text{ g}^{-1}$ ). The particle sizes of  $\text{Gd}_2\text{InSbO}_7$  and  $\text{Gd}_2\text{FeSbO}_7$  were uneven. We provide SEM images with low magnification of  $\text{Gd}_2\text{InSbO}_7$  and  $\text{Gd}_2\text{FeSbO}_7$ . Simultaneously, we give the TEM images of  $\text{Gd}_2\text{InSbO}_7$  and  $\text{Gd}_2\text{FeSbO}_7$ , which represent the average particle size. Because the particle size of  $\text{Gd}_2\text{InSbO}_7$  and  $\text{Gd}_2\text{FeSbO}_7$  compounds were greater than 230nm, their specific surface areas were less than  $5 \text{ m}^2 \text{ g}^{-1}$ .

There are three main reasons to choose Gd for producing  $\text{Gd}_2\text{FeSbO}_7$  and  $\text{Gd}_2\text{InSbO}_7$  in this paper. Firstly, the substitution of  $\text{Bi}^{3+}$  by  $\text{Gd}^{3+}$  and the substitution of  $\text{Ta}^{5+}$  by  $\text{Sb}^{5+}$  in  $\text{Bi}_2\text{InTaO}_7$  will produce smaller catalyst particles and increase the specific surface area, because the radii of  $\text{Gd}^{3+}$ ,  $\text{Bi}^{3+}$ ,  $\text{Ta}^{5+}$  and  $\text{Sb}^{5+}$  are 1.053 Å, 1.17 Å, 0.74 Å and 0.60 Å, which shows that the radius of  $\text{Gd}^{3+}$  is smaller than the radius of  $\text{Bi}^{3+}$ , and the radius of  $\text{Sb}^{5+}$  is smaller than the radius of  $\text{Ta}^{5+}$ . Similarly, the substitution of  $\text{Bi}^{3+}$  by  $\text{Gd}^{3+}$ , the substitution of  $\text{In}^{3+}$  by  $\text{Fe}^{3+}$  and the substitution of  $\text{Ta}^{5+}$  by  $\text{Sb}^{5+}$  in  $\text{Bi}_2\text{InTaO}_7$  will produce smaller catalyst particles and increase the specific surface area, because the radii of  $\text{In}^{3+}$  and  $\text{Fe}^{3+}$  are 0.92 Å and 0.78 Å, which shows that the radius of  $\text{Gd}^{3+}$  is smaller than the radius of  $\text{Bi}^{3+}$ , the radius of  $\text{Fe}^{3+}$  is smaller than the radius of  $\text{In}^{3+}$  and the radius of  $\text{Sb}^{5+}$  is smaller than the radius of  $\text{Ta}^{5+}$ . Thus, the active sites and the catalytic activity will increase. Secondly, the smaller catalyst particles probably result in a decrease of the migration distance of photogenerated electrons and holes, which are formed under visible light irradiation from the grain interior to reach the reaction site on the photocatalyst surface. Subsequently, the photogenerated electrons and the photogenerated holes that reach the surface of the particles in unit time increase, and the creation of more active sites is realized. As a result, it will probably improve the photocatalytic activities with decreasing the particle size of the photocatalyst. Thirdly, some literatures reported that Gd-containing catalyst had excellent catalytic performance [50–53].

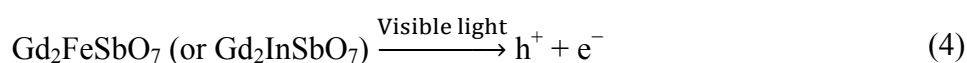
Figure 4 and Figure 5 show the action spectra of RhB degradation in the presence of  $\text{Gd}_2\text{FeSbO}_7$  or  $\text{Gd}_2\text{InSbO}_7$  under visible light irradiation. A clear photonic efficiency (0.03921% at its maximal point for  $\text{Gd}_2\text{FeSbO}_7$  and 0.03145% at its maximal point for  $\text{Gd}_2\text{InSbO}_7$ ) at wavelengths that corresponded to sub-Eg energies of the photocatalysts ( $\lambda$  from 425 to 800 nm) was observed for  $\text{Gd}_2\text{FeSbO}_7$  and  $\text{Gd}_2\text{InSbO}_7$ . The existence of photonic efficiency at energies where photons were not absorbed by the photocatalysts, and the correlation between the low-energy action spectrum and the absorption spectrum of RhB clearly demonstrated that any photodegradation at wavelengths above 479 nm should be attributed to the photosensitization by RhB dye itself, the mechanism showing as follows:



According to this mechanism, RhB adsorbed on  $\text{Gd}_2\text{FeSbO}_7$  or  $\text{Gd}_2\text{InSbO}_7$  was excited by visible light irradiation. Subsequently an electron was injected from the excited RhB to the conduction band

of  $\text{Gd}_2\text{FeSbO}_7$  or  $\text{Gd}_2\text{InSbO}_7$ , where the electron was scavenged by molecular oxygen. Scheme I served to explain the results obtained with  $\text{Gd}_2\text{FeSbO}_7$  or  $\text{Gd}_2\text{InSbO}_7$  as catalyst under visible light irradiation, where  $\text{Gd}_2\text{FeSbO}_7$  or  $\text{Gd}_2\text{InSbO}_7$  might serve to reduce recombination of photogenerated electrons and holes by scavenging of electrons [54].

The situation was different below 479 nm, where the photonic efficiency correlated well with the absorption spectra of  $\text{Gd}_2\text{FeSbO}_7$  and  $\text{Gd}_2\text{InSbO}_7$ . This result evidently showed that the mechanism, which was responsible for the photodegradation of RhB, went through band gap excitation of  $\text{Gd}_2\text{FeSbO}_7$  or  $\text{Gd}_2\text{InSbO}_7$ . Although detailed experiments about the effect of oxygen and water on the degradation mechanism were not performed, it was sensible to assume that the mechanism in the first steps was similar to the observed mechanism for  $\text{Gd}_2\text{FeSbO}_7$  or  $\text{Gd}_2\text{InSbO}_7$  under supra-bandgap irradiation, namely showing below:

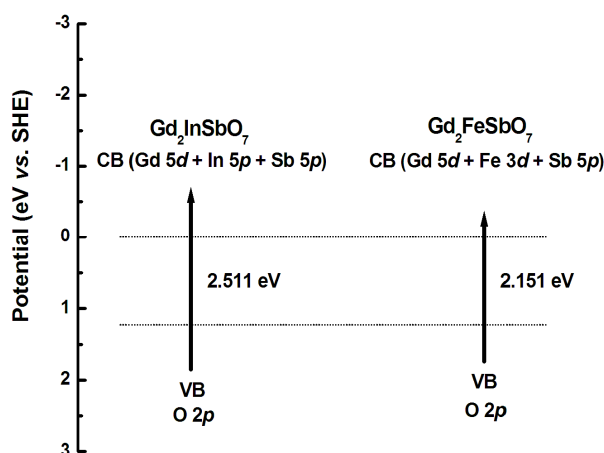


Previous luminescent studies had shown that the closer the M–O–M bond angle was to  $180^\circ$ , the more delocalized was the excited state [55]; As a result, the charge carriers could move easily in the matrix. The mobility of the photoinduced electrons and holes influenced the photocatalytic activity, because high diffusivity increased the probability that the photogenerated electrons and holes would reach the reactive sites of the catalyst surface. Based on the above results, the lattice parameter  $\alpha = 10.276026 \text{ \AA}$  for  $\text{Gd}_2\text{FeSbO}_7$  was smaller than the lattice parameter  $\alpha = 10.449546 \text{ \AA}$  for  $\text{Gd}_2\text{InSbO}_7$ , thus the photoinduced electrons and holes inside  $\text{Gd}_2\text{FeSbO}_7$  was easier and faster to reach the reactive sites of the  $\text{Gd}_2\text{FeSbO}_7$  surface than those inside  $\text{Gd}_2\text{InSbO}_7$ ; as a result, the photocatalytic degradation activity of  $\text{Gd}_2\text{FeSbO}_7$  was higher than that of  $\text{Gd}_2\text{InSbO}_7$ . Moreover, in this experiment, for  $\text{Gd}_2\text{FeSbO}_7$ , the Fe–O–Fe bond angle was  $116.424^\circ$ ; at the same time, for  $\text{Gd}_2\text{InSbO}_7$ , the In–O–In bond angle was  $123.338^\circ$ . The above results showed that the Fe–O–Fe bond angle of  $\text{Gd}_2\text{FeSbO}_7$  or the In–O–In bond angle of  $\text{Gd}_2\text{InSbO}_7$  was close to  $180^\circ$ , thus the photocatalytic activity of  $\text{Gd}_2\text{FeSbO}_7$  or  $\text{Gd}_2\text{InSbO}_7$  was accordingly higher. Moreover, the In–O–In bond angle of  $\text{Gd}_2\text{InSbO}_7$  was larger than the Fe–O–Fe bond angle of  $\text{Gd}_2\text{FeSbO}_7$ , which led to an increase of photocatalytic activity for  $\text{Gd}_2\text{InSbO}_7$  compared with that of  $\text{Gd}_2\text{FeSbO}_7$ . The crystal structures of  $\text{Gd}_2\text{FeSbO}_7$ ,  $\text{Gd}_2\text{InSbO}_7$  and  $\text{Bi}_2\text{InTaO}_7$  were the same, but their electronic structures were considered to be a little different. For  $\text{Gd}_2\text{FeSbO}_7$  or  $\text{Gd}_2\text{InSbO}_7$ , Sb or In was a  $5p$ -block metal element, Gd was a  $5d$ -block rare earth metal element and Fe was a  $3d$ -block metal element, but for  $\text{Bi}_2\text{InTaO}_7$ , Ta was a  $5d$ -block metal element and Bi was a  $6p$ -block metal element, indicating that the photocatalytic activity might be affected not only by the crystal structure of the photocatalysts, but also by the electronic structure of the photocatalysts. According to the above analysis, the difference of RhB photocatalytic degradation among  $\text{Gd}_2\text{FeSbO}_7$ ,  $\text{Gd}_2\text{InSbO}_7$  and  $\text{Bi}_2\text{InTaO}_7$  could be mainly attributed to the difference of their crystalline structure and electronic structure.

Figure 13 shows the suggested band structures of  $\text{Gd}_2\text{FeSbO}_7$  and  $\text{Gd}_2\text{InSbO}_7$ . The positions and width of the conduction band (CB) and the valence band (VB) were investigated by calculating the electronic band structure of  $\text{Gd}_2\text{FeSbO}_7$  and  $\text{Gd}_2\text{InSbO}_7$  with the plane-wave-based density functional

method. The band structure calculations of  $\text{Gd}_2\text{FeSbO}_7$  and  $\text{Gd}_2\text{InSbO}_7$  were performed with the program of Cambridge Serial Total Energy Package (CASTEP) and first-principles simulation. The CASTEP calculation was composed of the plane-wave pseudopotential total energy method according to the density functional theory. The generalized gradient approximation (GGA-PBE) and the geometry optimization were adopted. The selected unit cell for calculation was  $[\text{Gd}_2\text{FeSbO}_7]_2$  or  $[\text{Gd}_2\text{InSbO}_7]_2$ . The pseudo-atomic calculations were accomplished for  $\text{Gd}_2\text{FeSbO}_7$  with  $5d^16s^2$  (Gd),  $3d^64s^2$  (Fe),  $5s^25p^3$  (Sb) and  $2s^22p^4$  (O). The pseudo-atomic calculations were accomplished for  $\text{Gd}_2\text{InSbO}_7$  with  $5d^16s^2$  (Gd),  $5s^25p^1$  (In),  $5s^25p^3$  (Sb) and  $2s^22p^4$  (O). The self-consistent field tolerance was  $1.0 \times 10^{-6}$  eV/atom. The core electrons were replaced by the ultra-soft pseudopotentials. The FFT grid of the basis was  $40 \times 30 \times 30$ . The kinetic energy cutoff was 400 eV.  $4 \times 5 \times 5$  k-point, and the ultrasoft pseudopotential was applied in the above calculation. The total and partial density of the states of  $\text{Gd}_2\text{FeSbO}_7$  and  $\text{Gd}_2\text{InSbO}_7$  was taken into consideration. We determined the band structures of  $\text{Gd}_2\text{InSbO}_7$  and  $\text{Gd}_2\text{FeSbO}_7$  by borrowing ideas from the relevant literature [56–62]. Recently, the electronic structures of  $\text{InMO}_4$  ( $M = \text{V}, \text{Nb}$  and  $\text{Ta}$ ) and  $\text{BiVO}_4$  were reported by Oshikiri *et al.* based on the first principles calculations [63]. The conduction bands of  $\text{InMO}_4$  ( $M = \text{V}, \text{Nb}$  and  $\text{Ta}$ ) were mainly composed of a dominant  $d$  orbital component from V  $3d$ , Nb  $4d$  and Ta  $5d$  orbitals, respectively. The valence bands of  $\text{BiVO}_4$  were composed of a small Bi  $6s$  orbital component and a dominant O  $2p$  orbital component. The band structures of  $\text{Gd}_2\text{FeSbO}_7$  and  $\text{Gd}_2\text{InSbO}_7$  should be similar to that of the above compounds. Therefore, we concluded that the conduction band of  $\text{Gd}_2\text{FeSbO}_7$  was composed of Gd  $5d$ , Fe  $3d$  and Sb  $5p$  orbital components; meanwhile, the valence band of  $\text{Gd}_2\text{FeSbO}_7$  was composed of a small dominant O  $2p$  orbital component. Similarly, the conduction band of  $\text{Gd}_2\text{InSbO}_7$  was composed of Gd  $5d$ , In  $5p$  and Sb  $5p$  orbital components; moreover, the valence band of  $\text{Gd}_2\text{InSbO}_7$  was composed of a small dominant O  $2p$  orbital component. Direct absorption of photons by  $\text{Gd}_2\text{FeSbO}_7$  or  $\text{Gd}_2\text{InSbO}_7$  could produce electron–hole pairs within the catalyst, indicating that larger energy than the band gap of  $\text{Gd}_2\text{FeSbO}_7$  or  $\text{Gd}_2\text{InSbO}_7$  was necessary for decomposing RhB by photocatalysis.

**Figure 13.** Suggested band structures of  $\text{Gd}_2\text{FeSbO}_7$  and  $\text{Gd}_2\text{InSbO}_7$ .



The presented results indicated that the  $\text{Gd}_2\text{FeSbO}_7$  (or  $\text{Gd}_2\text{InSbO}_7$ )-visible light photocatalysis system might be regarded as a method for practical treatment of diluted colored waste water. Our  $\text{Gd}_2\text{FeSbO}_7$  (or  $\text{Gd}_2\text{InSbO}_7$ )-visible light photocatalysis system could be utilized for decolorization,

purification and detoxification in the textile, printing and dyeing industries within semi-arid countries. We designed  $\text{Gd}_2\text{FeSbO}_7$  (or  $\text{Gd}_2\text{InSbO}_7$ )-visible light photocatalysis system without demanding chemical reagents or using the high pressure of oxygen or heating. The decolorized and detoxified water was submitted to our new system for treatment, and the results showed that the  $\text{Gd}_2\text{FeSbO}_7$  (or  $\text{Gd}_2\text{InSbO}_7$ )-visible light photocatalysis system might provide a valuable treatment for purifying and reusing colored aqueous effluents.

### 3. Experimental Section

The novel photocatalysts were synthesized by a solid-state reaction method.  $\text{Gd}_2\text{O}_3$ ,  $\text{Bi}_2\text{O}_3$ ,  $\text{Fe}_2\text{O}_3$ ,  $\text{In}_2\text{O}_3$ ,  $\text{Sb}_2\text{O}_5$  and  $\text{Ta}_2\text{O}_5$  with purity of 99.99% (Sinopharm Group Chemical Reagent Co., Ltd., Shanghai, China) were used as starting materials. All powders were dried at 200 °C for 4 h before synthesis. For the sake of synthesizing  $\text{Gd}_2\text{FeSbO}_7$ , the precursors were stoichiometrically churned up, subsequently pressed into small columns and put into an alumina crucible (Shenyang Crucible Co., LTD, Shenyang, China). Eventually, calcination was performed at 1250 °C for 65 h in an electric furnace (KSL 1700X, Hefei Kejing Materials Technology CO., LTD, Hefei, China). Similarly,  $\text{Gd}_2\text{InSbO}_7$  was prepared by calcination at 1320 °C for 65 h, and  $\text{Bi}_2\text{InTaO}_7$  was prepared by calcination at 1050 °C for 46 h. The crystal structures of  $\text{Gd}_2\text{FeSbO}_7$  and  $\text{Gd}_2\text{InSbO}_7$  were analyzed by the powder X-ray diffraction method (D/MAX-RB, Rigaku Corporation, Tokyo, Japan) with  $\text{CuK}\alpha$  radiation ( $\lambda = 1.54056$  angstrom). The data were collected at 295 K with a step-scan procedure in the range of  $2\theta = 10\text{--}100^\circ$ . The step interval was  $0.02^\circ$ , and the time per step was 1.2 s. The chemical composition of  $\text{Gd}_2\text{InSbO}_7$  and  $\text{Gd}_2\text{FeSbO}_7$  was inspected by scanning electron microscope-X-ray energy dispersion spectrum (SEM-EDS, LEO 1530VP, LEO Electron Microscopy Inc., New York, NY, USA) and X-ray fluorescence spectrometer (XFS, ARL-9800, Thermo ARL, ARL Applied Research Laboratories S.A., Ecublens, Switzerland). The  $\text{Gd}^{3+}$  content,  $\text{Sb}^{5+}$  content,  $\text{Fe}^{3+}$  content,  $\text{In}^{3+}$  content and  $\text{O}^{2-}$  content of  $\text{Gd}_2\text{FeSbO}_7$  and  $\text{Gd}_2\text{InSbO}_7$  were detected by X-ray photoelectron spectroscopy (XPS, ESCALABMK-2, VG Scientific Ltd., East Grinstead, UK). The chemical composition within the depth profile of  $\text{Gd}_2\text{FeSbO}_7$  or  $\text{Gd}_2\text{InSbO}_7$  was examined by the argon ion denudation method when X-ray photoelectron spectroscopy was used. The optical absorption of  $\text{Gd}_2\text{FeSbO}_7$  and  $\text{Gd}_2\text{InSbO}_7$  was analyzed with an UV-visible spectrophotometer (Lambda 40, Perkin-Elmer Corporation, Waltham, MA, USA). The surface areas of  $\text{Gd}_2\text{InSbO}_7$ ,  $\text{Gd}_2\text{FeSbO}_7$  and  $\text{Bi}_2\text{InTaO}_7$  were surveyed by the Brunauer-Emmett-Teller (BET) method (MS-21, Quantachrome Instruments Corporation, Boynton Beach, FL, USA), with  $\text{N}_2$  adsorption at liquid nitrogen temperature. The particle sizes of the photocatalysts were measured by Malvern's mastersize-2000 particle size analyzer (Malvern Instruments Ltd, Worcestershire, United Kingdom). The particle morphology of  $\text{Gd}_2\text{FeSbO}_7$  and  $\text{Gd}_2\text{InSbO}_7$  were measured by transmission electron microscope (TEM, Tecnai F20 S-Twin, FEI Corporation, Hillsboro, OR, USA).

The photocatalytic degradation of rhodamine B (RhB) (Tianjin Kermel Chemical Reagent Co., Ltd., Tianjin, China) was performed with  $\text{Gd}_2\text{InSbO}_7$  or  $\text{Gd}_2\text{FeSbO}_7$  or  $\text{Bi}_2\text{InTaO}_7$  powder (0.8 g) suspended in RhB (300 mL 0.0293 mmol) solution by a pyrex glass cell (Jiangsu Yancheng Huaou Industry, Yancheng, China). Before visible light irradiation, the suspensions were magnetically stirred in darkness for 45 min to make sure the establishment of an adsorption/desorption equilibrium among

Gd<sub>2</sub>FeSbO<sub>7</sub>, Gd<sub>2</sub>InSbO<sub>7</sub>, Bi<sub>2</sub>InTaO<sub>7</sub>, the RhB dye and atmospheric oxygen. The photocatalytic reaction system was composed of a 300 W Xe arc lamp, which was a light resource, with the main emission wavelength at 436 nm (Nanjing JYZCPST CO., LTD, Nanjing, China), a magnetic stirrer and a cut-off filter ( $\lambda > 400$  nm, Jiangsu Nantong JSOL Corporation, Nantong, China). The Xe arc lamp was surrounded by a quartz jacket and was placed inside a photoreactor quartz vessel (5.8 cm in diameter and 68 cm in length) by which a suspension of RhB and the photocatalyst was circulated. An outer recycling water glass jacket maintained a near constant reaction temperature (22 °C), and the solution was stirred and aerated continuously. Two milliliters aliquots were sampled at various time intervals. The incident photon flux  $I_0$  measured by a radiometer (Model FZ-A, Photoelectric Instrument Factory Beijing Normal University, Beijing, China) was determined to be  $4.76 \times 10^{-6}$  Einstein L<sup>-1</sup> s<sup>-1</sup> under visible light irradiation (wavelength range of 400–700 nm). The incident photon flux on the photoreactor was varied by adjusting the distance between the photoreactor and the Xe arc lamp. The initial pH value of the liquid was 7.0 and was not adjusted subsequently. The concentration of RhB was determined based on the absorption at 553.5 nm measured by an UV-Vis spectrophotometer (Lambda 40, Perkin-Elmer Corporation, Waltham, MA, USA). The inorganic products obtained from RhB degradation were analyzed by ion chromatograph (DX-300, Dionex Corporation, Sunnyvale, CA, USA). The identification of RhB and the degradation intermediate products of RhB were performed by gas chromatograph—mass spectrometer (GC-MS, HP 6890 series gas chromatograph, AT<sup>TM</sup> column, 20.3 m × 0.32 mm, ID of 0.25 μm) operating at 320 °C, which was connected to a HP 5973 mass selective detector and a flame ionization detector, with H<sub>2</sub> as the carried gas. The intermediate products of RhB were measured by liquid chromatograph—mass spectrometer (LC-MS, Thermo Quest LCQ Duo, Atlanta, GA, USA, Beta Basic-C<sub>18</sub> HPLC column: 150 × 2.1 mm, ID of 5 μm, Finnigan, Thermo, Atlanta, GA, USA). Here, post-photocatalysis solution (20 μL) was injected automatically into the LC-MS system. The eluent contained 60% methanol and 40% water, and the flow rate was 0.2 mL min<sup>-1</sup>. MS conditions included an electrospray ionization interface, a capillary temperature of 27 °C with a voltage of 19.00 V, a spray voltage of 5000 V and a constant sheath gas flow rate. The spectrum was acquired in the negative ion scan mode, sweeping the  $m/z$  range from 50 to 600. Evolution of CO<sub>2</sub> was analyzed with an intersmat<sup>TM</sup> IGC120-MB gas chromatograph equipped with a porapack Q column (3 m in length and an inner diameter of 0.25 in.), which was connected to a catharometer detector.

The total organic carbon (TOC) concentration was determined with a TOC analyzer (TOC-5000, Shimadzu Corporation, Kyoto, Japan). The photonic efficiency was calculated according to the following equation [64]:

$$\xi = R / I_0 \quad (7)$$

where  $\phi$  was the photonic efficiency (%),  $R$  was the rate of RhB degradation (Mol L<sup>-1</sup> s<sup>-1</sup>) and  $I_0$  was the incident photon flux (Einstein L<sup>-1</sup> s<sup>-1</sup>).

#### 4. Conclusions

Gd<sub>2</sub>FeSbO<sub>7</sub> and Gd<sub>2</sub>InSbO<sub>7</sub> were prepared by the solid-state reaction method for the first time. The structural, optical absorption and photocatalytic properties of Gd<sub>2</sub>FeSbO<sub>7</sub> and Gd<sub>2</sub>InSbO<sub>7</sub> were investigated and compared with Bi<sub>2</sub>InTaO<sub>7</sub>. XRD results indicated that Gd<sub>2</sub>FeSbO<sub>7</sub> and Gd<sub>2</sub>InSbO<sub>7</sub>

crystallized with the pyrochlore-type structure, cubic crystal system and space group  $Fd3m$ . The lattice parameters of  $Gd_2FeSbO_7$  and  $Gd_2InSbO_7$  were found to be  $a = 10.276026 \text{ \AA}$  and  $a = 10.449546 \text{ \AA}$ . The band gaps of  $Gd_2FeSbO_7$  and  $Gd_2InSbO_7$  were estimated to be about 2.151 eV and 2.897 eV, indicating that  $Gd_2FeSbO_7$  and  $Gd_2InSbO_7$  showed a strong optical absorption in the visible light region ( $\lambda > 400 \text{ nm}$ ). Photocatalytic degradation of aqueous RhB was observed under visible light irradiation in the presence of  $Gd_2FeSbO_7$  and  $Gd_2InSbO_7$  accompanied with the formation of final products, such as  $CO_2$  and water. Complete removal of carbon from RhB was obtained, as indicated from TOC and  $CO_2$  yield measurements, with  $Gd_2FeSbO_7$  or  $Gd_2InSbO_7$  as catalyst under visible light irradiation. A  $Gd_2FeSbO_7$  or ( $Gd_2InSbO_7$ ) visible light photocatalysis system could be regarded as an effective way for treating textile industry wastewater.  $Gd_2FeSbO_7$  or  $Gd_2InSbO_7$  also showed higher photocatalytic activity compared with  $Bi_2InTaO_7$  for RhB photocatalytic degradation under visible light irradiation. Moreover,  $Gd_2FeSbO_7$  exhibited higher catalytic activity than  $Gd_2InSbO_7$ . The photocatalytic degradation of RhB was in line with the first-order reaction kinetics. The apparent first-order rate constant  $k$  was 0.01606, 0.02220 and 0.00318  $\text{min}^{-1}$  with  $Gd_2FeSbO_7$ ,  $Gd_2InSbO_7$  or  $Bi_2InTaO_7$  as catalyst. The possible photocatalytic degradation pathway of RhB was proposed under visible light irradiation.

## Acknowledgments

This work was supported by the National Natural Science Foundation of China (No. 21277067). This work was supported by a grant from the China-Israel Joint Research Program in Water Technology and Renewable Energy (No. 5). This work was supported by a grant from The Fourth Technological Development Scheming (Industry) Program of Suzhou City of China from 2010 (SYG201006). This work was supported by a grant from the Fundamental Research Funds for the Central Universities.

## References

1. Bhatnagar, A.; Jain, A.K. A comparative adsorption study with different industrial wastes as adsorbents for the removal of cationic dyes from water. *J. Colloid Interface Sci.* **2005**, *281*, 49–55.
2. Fu, H.B.; Pan, C.S.; Yao, W.Q.; Zhu, Y.F. Visible-light-induced degradation of rhodamine B by nanosized  $Bi_2WO_6$ . *J. Phys. Chem. B* **2005**, *109*, 22432–22439.
3. Guo, Y.P.; Zhao, J.Z.; Zhang, H.; Yang, S.F.; Qi, J.R.; Wang, Z.C.; Xu, H.D. Use of rice husk-based porous carbon for adsorption of Rhodamine B from aqueous solutions. *Dyes Pigm.* **2005**, *66*, 123–128.
4. Gupta, V.K.; Ali, I.; Saini, V.K. Removal of rhodamine B, fast green and methylene blue from wastewater using red mud, an aluminum industry waste. *Ind. Eng. Chem. Res.* **2004**, *43*, 1740–1747.
5. Fujii, T.; Nishikiori, H.; Tamura, T. Absorption-Spectra of Rhodamine-B dimers in dip-coated thin-films prepared by the sol-gel method. *Chem. Phys. Lett.* **1995**, *233*, 424–429.
6. Wang, S.B.; Li, H.T. Dye adsorption on unburned carbon: Kinetics and equilibrium. *J. Hazard. Mater.* **2005**, *126*, 71–77.

7. Wang, S.B.; Boyjoo, Y.; Choueib, A. A comparative study of dye removal using fly ash treated by different methods. *Chemosphere* **2005**, *60*, 1401–1407.
8. Gupta, V.K.; Jain, R.; Malathi, S.; Nayak, A. Adsorption-desorption studies of indigocarmine from industrial effluents by using deoiled mustard and its comparison with charcoal. *J. Colloid Interface Sci.* **2010**, *348*, 628–633.
9. Ohsaki, H.; Kanai, N.; Fukunaga, Y.; Suzuki, M.; Watanabe, T.; Hashimoto, K. Photocatalytic properties of SnO<sub>2</sub>/TiO<sub>2</sub> multilayers. *Thin Solid Films* **2006**, *502*, 138–142.
10. Davit, P.; Martra, G.; Coluccia, S.; Augugliaro, V.; Lopez, E.G.; Loddo, V.; Marci, G.; Palmisano, L.; Schiavello, M. Adsorption and photocatalytic degradation of acetonitrile: FT-IR investigation. *J. Mol. Catal. A* **2003**, *204*, 693–701.
11. Kim, S.; Choi, W. Dual photocatalytic pathways of trichloroacetate degradation on TiO<sub>2</sub>: Effects of nanosized platinum deposits on kinetics and mechanism. *J. Phys. Chem. B* **2002**, *106*, 13311–13317.
12. Luan, J.F.; Ma, K.; Wang, S.; Hu, Z.T.; Li, Y.M.; Pan, B.C. Research on Photocatalytic Degradation Pathway and Degradation Mechanisms of Organics. *Curr. Org. Chem.* **2010**, *14*, 645–682.
13. Chatterjee, D.; Mahata, A. Visible light induced photodegradation of organic pollutants on dye adsorbed TiO<sub>2</sub> surface. *J. Photochem. Photobiol. A* **2002**, *153*, 199–204.
14. Fabbri, D.; Prevot, A.B.; Zelano, V.; Ginepro, M.; Pramauro, E. Removal and degradation of aromatic compounds from a highly polluted site by coupling soil washing with photocatalysis. *Chemosphere* **2008**, *71*, 59–65.
15. Sohrabi, M.R.; Ghavami, M. Comparison of Direct Yellow 12 dye degradation efficiency using UV/semiconductor and UV/H(2)O(2)/semiconductor systems. *Desalination* **2010**, *252*, 157–162.
16. Franch, M.I.; Peral, J.; Domenech, X.; Howe, R.F.; Ayllon, J.A. Enhancement of photocatalytic activity of TiO<sub>2</sub> by adsorbed aluminium(III). *Appl. Catal. B* **2005**, *55*, 105–113.
17. Yamashita, H.; Nose, H.; Kuwahara, Y.; Nishida, Y.; Yuan, S.; Mori, K. TiO<sub>2</sub> photocatalyst loaded on hydrophobic Si<sub>3</sub>N<sub>4</sub> support for efficient degradation of organics diluted in water. *Appl. Catal. A* **2008**, *350*, 164–168.
18. Neppolian, B.; Yamashita, H.; Okada, Y.; Nishijima, H.; Anpo, M. Preparation of unique TiO<sub>2</sub> nano-particle photocatalysts by a multi-gelation method for control of the physicochemical parameters and reactivity. *Catal. Lett.* **2005**, *105*, 111–117.
19. An, H.Q.; Zhou, J.; Li, J.X.; Zhu, B.L.; Wang, S.R.; Zhang, S.M.; Wu, S.H.; Huang, W.P. Deposition of Pt on the stable nanotubular TiO<sub>2</sub> and its photocatalytic performance. *Catal. Commun.* **2009**, *11*, 175–179.
20. Davit, P.; Martra, G.; Coluccia, S. Photocatalytic degradation of organic compounds on TiO<sub>2</sub> powders: FT-IR investigation of surface reactivity and mechanistic aspects. *J. Jpn. Pet. Inst.* **2004**, *47*, 359–376.
21. Cernigoj, U.; Stangar, U.L.; Trebse, P. Degradation of neonicotinoid insecticides by different advanced oxidation processes and studying the effect of ozone on TiO<sub>2</sub> photocatalysis. *Appl. Catal. B* **2007**, *75*, 229–238.
22. Sohrabi, M.R.; Ghavami, M. Photocatalytic degradation of Direct Red 23 dye using UV/TiO<sub>2</sub>: Effect of operational parameters. *J. Hazard. Mater.* **2008**, *153*, 1235–1239.

23. Franch, M.I.; Peral, J.; Domenech, X.; Ayllon, J.A. Aluminium(III) adsorption: A soft and simple method to prevent TiO<sub>2</sub> deactivation during salicylic acid photodegradation. *Chem. Commun.* **2005**, *14*, 1851–1853.
24. Hammami, S.; Bellakhal, N.; Oturan, N.; Oturan, M.A.; Dachraoui, M. Degradation of Acid Orange 7 by electrochemically generated (OH)-O-center dot radicals in acidic aqueous medium using a boron-doped diamond or platinum anode: A mechanistic study. *Chemosphere* **2008**, *73*, 678–684.
25. Luan, J.F.; Pan, B.C.; Paz, Y.; Li, Y.M.; Wu, X.S.; Zou, Z.G. Structural, photophysical and photocatalytic properties of new Bi<sub>2</sub>SbVO<sub>7</sub> under visible light irradiation. *Phys. Chem. Chem. Phys.* **2009**, *11*, 6289–6298.
26. Arana, J.; Rendon, E.T.; Rodriguez, J.M.D.; Melian, J.A.H.; Diaz, O.G.; Pena, J.P. FTIR study of the photocatalytic degradation of NH<sup>4+</sup> determination wastes. *J. Photochem. Photobiol. A* **2002**, *148*, 215–222.
27. Arana, J.; Nieto, J.L.M.; Melian, J.A.H.; Rodriguez, J.M.D.; Diaz, O.G.; Pena, J.P.; Bergasa, O.; Alvarez, C.; Mendez, J. Photocatalytic degradation of formaldehyde containing wastewater from veterinarian laboratories. *Chemosphere* **2004**, *55*, 893–904.
28. Vijayabalan, A.; Selvam, K.; Velmurugan, R.; Swaminathan, M. Photocatalytic activity of surface fluorinated TiO<sub>2</sub>-P25 in the degradation of Reactive Orange 4. *J. Hazard. Mater.* **2009**, *172*, 914–921.
29. Arana, J.; Rodriguez, J.M.D.; Diaz, O.G.; Melian, J.A.H.; Pena, J.P. Comparative study on the photocatalytic mineralization of homologous aliphatic acids and alcohols. *Appl. Surface Sci.* **2006**, *252*, 8193–8202.
30. Eslami, A.; Nasser, S.; Yadollahi, B.; Mesdaghinia, A.; Vaezi, F.; Nabizadeh, R.; Nazmara, S. Photocatalytic degradation of methyl tert-butyl ether (MTBE) in contaminated water by ZnO nanoparticles. *J. Chem. Technol. Biotechnol.* **2008**, *83*, 1447–1453.
31. Arana, J.; Cabo, C.G.I.; Rodriguez, C.F.; Melian, J.A.H.; Mendez, J.A.O.; Rodriguez, J.M.D.; Pena, J.P. Combining TiO<sub>2</sub>-photocatalysis and wetland reactors for the efficient treatment of pesticides. *Chemosphere* **2008**, *71*, 788–794.
32. Li, J.P.; Zhang, X.; Ai, Z.H.; Jia, F.L.; Zhang, L.Z.; Lin, J. Efficient visible light degradation of rhodamine B by a photo-electrochemical process based on a Bi<sub>2</sub>WO<sub>6</sub> nanoplate film electrode. *J. Phys. Chem. C* **2007**, *111*, 6832–6836.
33. Li, X.; Ye, J.H. Photocatalytic degradation of rhodamine B over Pb<sub>3</sub>Nb<sub>4</sub>O<sub>13</sub>/fumed SiO<sub>2</sub> composite under visible light irradiation. *J. Phys. Chem. C* **2007**, *111*, 13109–13116.
34. Wu, J.M. Photodegradation of rhodamine B in water assisted by titania nanorod thin films subjected to various thermal treatments. *Environ. Sci. Technol.* **2007**, *41*, 1723–1728.
35. Wu, J.M.; Zhang, T.W. Photodegradation of rhodamine B in water assisted by titania films prepared through a novel procedure. *J. Photochem. Photobiol. A* **2004**, *162*, 171–177.
36. Li, J.Q.; Li, L.P.; Zheng, L.; Xian, Y.Z.; Jin, L.T. Photoelectrocatalytic degradation of rhodamine B using Ti/TiO<sub>2</sub> electrode prepared by laser calcination method. *Electrochim. Acta* **2006**, *51*, 4942–4949.

37. Qu, P.; Zhao, J.C.; Shen, T.; Hidaka, H. TiO<sub>2</sub>-assisted photodegradation of dyes: A study of two competitive primary processes in the degradation of RB in an aqueous TiO<sub>2</sub> colloidal solution. *J. Mol. Catal. A* **1998**, *129*, 257–268.
38. Zhao, J.C.; Wu, T.X.; Wu, K.Q.; Oikawa, K.; Hidaka, H.; Serpone, N. Photoassisted degradation of dye pollutants. 3. Degradation of the cationic dye rhodamine B in aqueous anionic surfactant/TiO<sub>2</sub> dispersions under visible light irradiation: Evidence for the need of substrate adsorption on TiO<sub>2</sub> particles. *Environ. Sci. Technol.* **1998**, *32*, 2394–2400.
39. Luan, J.F.; Ma, K.; Zhang, L.Y.; Li, M.; Li, Y.M.; Pan, B.C. Research on Different Preparation Methods of New Photocatalysts. *Curr. Org. Chem.* **2010**, *14*, 683–698.
40. Kitano, M.; Takeuchi, M.; Matsuoka, M.; Thomas, J.M.; Anpo, M. Preparation of visible light-responsive TiO<sub>2</sub> thin film photocatalysts by an RF magnetron sputtering deposition method and their photocatalytic reactivity. *Chem. Lett.* **2005**, *34*, 616–617.
41. Anpo, M.; Yamashita, H.; Ikeue, K.; Fujii, Y.; Zhang, S.G.; Ichihashi, Y.; Park, D.R.; Suzuki, Y.; Koyano, K.; Tatsumi, T. Photocatalytic reduction of CO<sub>2</sub> with H<sub>2</sub>O on Ti-MCM-41 and Ti-MCM-48 mesoporous zeolite catalysts. *Catal. Today* **1998**, *44*, 327–332.
42. Anpo, M.; Takeuchi, M. The design and development of highly reactive titanium oxide photocatalysts operating under visible light irradiation. *J. Catal.* **2003**, *216*, 505–516.
43. Hamadani, M.; Reisi-Vanani, A.; Majedi, A. Preparation and characterization of S-doped TiO<sub>2</sub> nanoparticles, effect of calcination temperature and evaluation of photocatalytic activity. *Mater. Chem. Phys.* **2009**, *116*, 376–382.
44. Luan, J.F.; Zhao, W.; Feng, J.W.; Cai, H.L.; Zheng, Z.; Pan, B.C.; Wu, X.S.; Zou, Z.G.; Li, Y.M. Structural, photophysical and photocatalytic properties of novel Bi<sub>2</sub>AlVO<sub>7</sub>. *J. Hazard. Mater.* **2009**, *164*, 781–789.
45. Izumi, F. A software package for the Rietveld analysis of X-ray and neutron diffraction patterns. *J. Crystallogr. Assoc. Jpn.* **1985**, *27*, 23–26.
46. Zou, Z.; Ye, J.; Arakawa, H. Preparation, structural and photophysical properties of Bi<sub>2</sub>InNbO<sub>7</sub> compound. *J. Mater. Sci. Lett.* **2000**, *19*, 1909–1911.
47. Tauc, J.; Grigorov, R.; Vancu, A. Optical properties and electronic structure of amorphous germanium. *Phys. Status Solidi* **1966**, *15*, 627–637.
48. Butler, M.A. Photoelectrolysis and physical-properties of semiconducting electrode WO<sub>3</sub>. *J. Appl. Phys.* **1977**, *48*, 1914–1920.
49. Horikoshi, S.; Saitou, A.; Hidaka, H.; Serpone, N. Environmental remediation by an integrated microwave/UV illumination method. V. Thermal and nonthermal effects of microwave radiation on the photocatalyst and on the photodegradation of rhodamine-b under UV/Vis radiation. *Environ. Sci. Technol.* **2003**, *37*, 5813–5822.
50. Li, G.R.; Qu, D.L.; Arurault, L.; Tong, Y.X. Hierarchically Porous Gd<sup>3+</sup>-Doped CeO<sub>2</sub> Nanostructures for the Remarkable Enhancement of Optical and Magnetic Properties. *J. Phys. Chem. C* **2009**, *113*, 1235–1241.
51. Selvan, R.K.; Gedanken, A.; Anilkumar, P.; Manikandan, G.; Karunakaran, C. Synthesis and Characterization of Rare Earth Orthovanadate (RVO<sub>4</sub>; R = La, Ce, Nd, Sm, Eu & Gd) Nanorods/Nanocrystals/Nanospindles by a Facile Sonochemical Method and Their Catalytic Properties. *J. Cluster Sci.* **2009**, *20*, 291–305.

52. Perles, J.; Fortes-Revilla, C.; Gutierrez-Puebla, E.; Iglesias, M.; Monge, M.A.; Ruiz-Valero, C.; Snejko, N. Synthesis, structure and catalytic properties of rare-earth ternary sulfates. *Chem. Mater.* **2005**, *17*, 2701–2706.
53. Wang, W.; Su, C.; Ran, R.; Shao, Z.P. A new Gd-promoted nickel catalyst for methane conversion to syngas and as an anode functional layer in a solid oxide fuel cell. *J. Power Sources* **2011**, *196*, 3855–3862.
54. Nasr, C.; Vinodgopal, K.; Fisher, L.; Hotchandani, S.; Chattopadhyay, A.K.; Kamat, P.V. Environmental photochemistry on semiconductor surfaces. Visible light induced degradation of a textile diazo dye, naphthol blue black, on TiO<sub>2</sub> nanoparticles. *J. Phys. Chem.* **1996**, *100*, 8436–8442.
55. Wiegel, M.; Middel, W.; Blasse, G. Influence of NS<sub>2</sub> ions on the luminescence of niobates and tantalates. *J. Mater. Chem.* **1995**, *5*, 981–983.
56. Li, N.; Xiao, H.Y.; Zu, X.T.; Wang, L.M.; Ewing, R.C.; Lian, J.; Gao, F. First-principles study of electronic properties of La<sub>2</sub>Hf<sub>2</sub>O<sub>7</sub> and Gd<sub>2</sub>Hf<sub>2</sub>O<sub>7</sub>. *J. Appl. Phys.* **2007**, *102*, 063704:1–063704:6.
57. Luan, J.F.; Zhang, L.Y.; Ma, K.; Li, Y.M.; Zou, Z.G. Preparation and property characterization of new Y<sub>2</sub>FeSbO<sub>7</sub> and In<sub>2</sub>FeSbO<sub>7</sub> photocatalysts. *Solid State Sci.* **2011**, *13*, 185–194.
58. Charifi, Z.; Reshak, A.H.; Baaziz, H. Phase transition of LaX (X = P, As, Sb and Bi) at high pressure: Theoretical investigation of the structural and electronic properties. *Solid State Commun.* **2008**, *148*, 139–144.
59. Vajenine, G.V.; Hoffmann, R.; zurLoye, H.C. The electronic structures and magnetic properties of one-dimensional ABO<sub>6</sub> chains in Sr<sub>3</sub>ABO<sub>6</sub> (A = Co, Ni; B = Pt, Ir) and two-dimensional MO<sub>3</sub> sheets in InMO<sub>3</sub> (M = Fe, Mn). *Chem. Phys.* **1996**, *204*, 469–478.
60. Luo, H.Z.; Zhu, Z.Y.; Liu, G.D.; Xu, S.F.; Wu, G.H.; Liu, H.Y.; Qu, J.P.; Li, Y.X. *Ab-initio* investigation of electronic properties magnetism of half-Heusler alloys XCrAl (X = Fe, Co, Ni) and NiCrZ (Z = Al, Ga, In). *Phys. B Condens. Matter* **2008**, *403*, 200–206.
61. Xiang, H.P.; Wu, Z.J.; Meng, J. Theoretical investigation on the magnetic and electronic properties of Sr<sub>2</sub>BMoO<sub>6</sub> (B = Fe, Co). *Phys. Status Solidi B* **2005**, *242*, 1414–1421.
62. Zhou, A.; Liu, L.S.; Shu, C.C.; Zhai, P.C.; Zhao, W.Y.; Zhang, Q.J. Electronic Structures and Transport Properties of RFe<sub>4</sub>Sb<sub>12</sub> (R = Na, Ca, Nd, Yb, Sn, In). *J. Electron. Mater.* **2011**, *40*, 974–979.
63. Oshikiri, M.; Boero, M.; Ye, J.H.; Zou, Z.G.; Kido, G. Electronic structures of promising photocatalysts InMO<sub>4</sub> (M = V, Nb, Ta) and BiVO<sub>4</sub> for water decomposition in the visible wavelength region. *J. Chem. Phys.* **2002**, *117*, 7313–7318.
64. Marugan, J.; Hufschmidt, D.; Sagawe, G.; Selzer, V.; Bahnemann, D. Optical density and photonic efficiency of silica-supported TiO<sub>2</sub> photocatalysts. *Water Res.* **2006**, *40*, 833–839.